Photon-modulated linear and nonlinear anomalous Hall effects in type-II semi-Dirac semimetals

Jin-Na Chen, Yan-Yan Yang, Yong-Long Zhou, Yong-Jia Wu, Hou-Jian Duan, Ming-Xun Deng [*] and Rui-Qiang Wang [†]

Guangdong Provincial Key Laboratory of Quantum Engineering and Quantum Materials, School of Physics and Telecommunication Engineering, South China Normal University, Guangzhou 510006, China
and Guangdong-Hong Kong Joint Laboratory of Quantum Matter, South China Normal University, Guangzhou 510006, China

Two-dimensional semi-Dirac materials, with quadratic dispersion in one direction and linear dispersion in the orthogonal direction, provide a route to formation of the Chern-insulating states in solids. Within the framework of the Floquet theory, we investigate the photon-modulated linear and nonlinear anomalous Hall effect (AHE) in type-II semi-Dirac semimetals and find that rich topological phases, as well as interesting phenomena related to the topological transitions, can be realized and manipulated by circularly polarized light (CPL). By tuning the CPL parameters, we can control the local inverted gaps independently and switch the system between different topological phases optionally. We also demonstrate that, when the Fermi level locates outside the gap, the Drude component of the conductivity can contribute to the AHE as well, because of the anisotropy of the electronic structure. Besides, the nonlinear Hall effect due to the Berry curvature dipole can be observable when the inversion symmetry between opposite valleys is broken. Our findings are helpful to understand the topological properties of the emergent type-II semi-Dirac semimetals.

I. INTRODUCTION

The anomalous Hall effect (AHE), discovered a century ago, where current flows orthogonal to an applied electric field without an external magnetic field, is one of the most fundamental and extensively studied phenomena in physics [1]. The AHE in solids with spontaneous broken time-reversal (TR) symmetry, typically in a ferromagnetic phase, can arise from intrinsic and extrinsic mechanisms [2–5]. The intrinsic AHE is an intrinsic quantum-mechanical property of a perfect crystal [6–9], governed by the electronic structure of a material that causes an electron to acquire a transverse velocity as it travels in-between scattering events. The extrinsic mechanisms depend on electrons scattering off sudden changes in the periodic potential of crystals, e.g., side jump or skew scattering from disorder caused by structural defects or chemical and magnetic impurities [3,4,10–16]. Recently, there has been a surge of interest in the exploration of nonspontaneous AHEs, in which the TR symmetry is broken by an external magnetic field, while the resulting Hall response is not commensurate with the magnitude of the applied field, making it distinct from the ordinary Hall effect [17,18]. The great theoretical and experimental advances of the AHE in varied systems, especially in topological materials [19–21], have led to an explosion of activities in the field of condensed matter [22–35].

Topological insulators are novel quantum states of matter, which appear as conductors in the boundaries but as insulators in the bulk. The boundary states are protected by the topological invariants of bulk states [19,20] and manifest in the

transport as a quantized anomalous Hall (QAH) conductivity $\sigma_{xy} = C e^2/h$ when the Fermi level lies in the bulk band gap, where C is an integer topological index known as the Chern number [36,37]. The QAH state can be realized in several materials, such as in the magnetically doped topological insulators [22,23,38], honeycomb [39–42], or square lattices [43–45] formed by transition-metal and heavy-metal ions.

Recently, a class of two-dimensional systems, named the semi-Dirac semimetals (SDSMs) [46–50], has been proposed, in which the bands disperse differently in two orthogonal directions, i.e., linearly in one direction and quadratically in the other. The strained black phosphorus [51], organic conductor α-$(BEDT - TTF)_2 I_3$ [52], dielectric photonic systems [53] and hexagonal lattices in the presence of a magnetic field [54] were demonstrated to be of the SDSM dispersion. The semi-Dirac structures can be divided into two qualitatively different types, namely, type-I and type-II SDSMs. The former, proposed in Refs. [47–50], cannot lead to the QAH state. The latter, as discussed in Ref. [50], is a QAH insulator with the spin-orbit coupling included, which can be realized in the TiO_2/VO_2 nanostructure [47–50]. The type-II SDSMs provide a route to formation of the Chern-insulating states.

Different from type-I SDSMs and conventional Dirac materials, the Dirac mass of type-II SDSMs is momentum dependent. As a result, their topological properties depend strongly on location of the Dirac points in momentum space, because the Berry curvatures can change sign as the Dirac points move in momentum space. On the other hand, there can be multiple Dirac points around a single subvalley of the type-II SDSMs, the interplay between which could induce interesting physical phenomena. Accordingly, by manipulation of the location of the Dirac points and interplay between them, rich topological phases could be expected. However,

*dengmingxun@scnu.edu.cn
†wangruiqiang@m.scnu.edu.cn

since the inverted gaps around the local Dirac points are the same in magnitude for a constant Dirac mass, the closing and reopening of them are always synchronously. Thus, the total Chern number is either positive or negative 2, which depends only on the sign of the Dirac mass, and as a result, the varied topological phases cannot be well distinguished.

One of the powerful approaches to manipulate the electronic structure is by utilization of polarized light. The laser-induced AHE was theorized by Oka and Aoki in graphene [55], followed by which considerable attentions have been paid to the light-induced topological transitions in solid states [56–68], as well as the dissipative effects [69,70] and validity of the bulk-boundary correspondence [71,72] in a Floquet system. Recently, the laser-induced AHE predicted in graphene has been experimentally probed by McIver *et al.* [73], which confirms that the topological phase transitions can be modulated by circularly polarized light (CPL). Additionally, when the Fermi level is out of the gap, the Berry curvature dipole could contribute a Hall current $\propto E^2$, which is named the nonlinear Hall effect [74–80], where E denotes the external electric field. The nonlinear Hall effect is quite sensitive to the electronic structure and it can exist in systems with TR symmetry, but generally requires breaking the inversion symmetry. With the electronic structure driven by the polarized light, both the linear and nonlinear Hall effect would exhibit new characters, the study of which is beneficial to understand the topological properties of the emergent type-II SDSMs.

In this paper, we investigate the photon-modulated linear and nonlinear AHE in type-II SDSMs by using the Floquet theory. It is found that the rich topological phases within the type-II SDSMs can be well distinguished and controllable by the CPL. Since the Dirac points in the x and y axes respond differently to the CPL, we can manipulate the local inverted gaps independently, and so switch the system between different topological phases optionally. As a result, the QAH plateau within the bulk band gap can be tunable from $-6e^2/h$ to $6e^2/h$. Moreover, the interplay between the multiple Dirac points can be regulated by the CPL, leading to anomalous behaviors in the anomalous Hall conductivity. While the Berry-curvature-induced AHE is strongly suppressed as the Fermi level locates outside the gap, the Drude component of the conductivity can also contribute to the AHE, which is modulated by the incident direction of the CPL. Besides, we predict the existence of the nonlinear Hall effect in type-II SDSMs, because of the nonvanishing Berry curvature dipole. The nonlinear Hall effect can be observable when the inversion symmetry between opposite valleys is broken. The rest of this paper is organized as follows. In Sec. II, we introduce the model and method. The CPL-modulated linear and nonlinear AHE are discussed respectively in Secs. III and IV, and the last section contains a summary.

II. MODEL AND METHOD

We begin with a model for type-II SDSMs, whose Hamiltonian is given by

$$H(\boldsymbol{k}) = \left(\beta k_x^2 - v_F k_y - \delta_0\right)\sigma_x + \alpha k_x k_y \sigma_y + m_z \sigma_z, \quad (1)$$
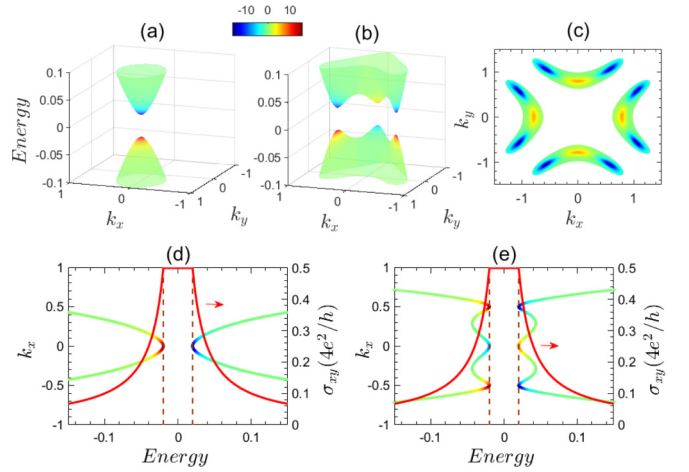

FIG. 1. (a), (b) The energy dispersion with the filled colors indicating the value of the Berry curvature, (c) top view of the conduction band below $\varepsilon_{\boldsymbol{k},+} = E_F$, and (d), (e) Hall conductivity (right axis) in the absence of the CPL for $m_z > 0$. The dispersion (left axis) in (d) and (e) is plotted along the parabola $k_y = (\beta k_x^2 - \delta_0)/v_F$. For comparing, we set $\delta_0 < 0$ in (a) and (d), while $\delta_0 > 0$ in (b), (c), and (e).

where $\boldsymbol{\sigma} = (\sigma_x, \sigma_y, \sigma_z)$ is the vector of Pauli matrix, $\hbar^2/(2\beta)$ corresponds to the Newtonian mass of the quasiparticle along the x direction, and m_z accounts for the Dirac mass. The type-II semi-Dirac model can be used to describe the low-energy electronic structure of the TiO$_2$/VO$_2$ nanostructure [47–50]. In Eq. (1), we present only one of the four valleys, as they are related to each other by fourfold rotations [50]. Diagonalizing $H(\boldsymbol{k})$ yields the dispersion

$$\varepsilon_{\boldsymbol{k},s} = s\sqrt{\left(\beta k_x^2 - v_F k_y - \delta_0\right)^2 + (\alpha k_x k_y)^2 + m_z^2} \quad (2)$$

with $s = \pm$ for the conduction/valence band. For convenience, we assume $\alpha, \beta > 0$. In Figs. 1(a) and 1(b), we display the numerical results for the energy spectrum. In the absence of the Dirac mass, i.e., $m_z = 0$, the conduction and valence bands touch at a Dirac point $Y = (0, -\delta_0/v_F)$ in the y axis and a pair of Dirac points $X_{\pm} = (\pm\sqrt{\delta_0/\beta}, 0)$ in the x axis when $\delta_0 > 0$. As $\delta_0 < 0$, the Dirac points $X_{\pm}$ will be gapped out. For a finite constant m_z, no Dirac points survive. The gap closing and reopening are usually related to a topological transition. Accordingly, by tuning the Dirac mass and δ_0, abundant topological phases and interesting phenomena associated with the topological transitions could be expected in this system.

In practice, a feasible way to regulate the electronic structure is by means of light. As the sample is driven by a beam of CPL, the behavior of the quasiparticles can be described by a time-dependent Hamiltonian $\mathcal{H}(\boldsymbol{k}, t) = H(\boldsymbol{k} + e\boldsymbol{A}/\hbar)$, where $\boldsymbol{A}(t) = A_0[\sin(\omega t)\boldsymbol{e}_1 - \sin(\omega t + \varphi)\boldsymbol{e}_2]$ is the vector potential for the light of amplitude A_0 and frequency ω. The phase φ is adopted to characterize the polarization, for instance, $\varphi = 0$ and $\varphi = \pm\pi/2$ correspond respectively to the linearly and right/left polarization. Here, $\boldsymbol{e}_1 = (\cos\theta\cos\phi, \cos\theta\sin\phi, -\sin\theta)$ and $\boldsymbol{e}_2 = (\sin\phi, -\cos\phi, 0)$, satisfying $\boldsymbol{e}_1 \cdot \boldsymbol{e}_2 = 0$, are two unit vectors perpendicular to the incident direction $\boldsymbol{e}_{\text{in}} = (\sin\theta\cos\phi, \sin\theta\sin\phi, \cos\theta)$ of the light. Following the
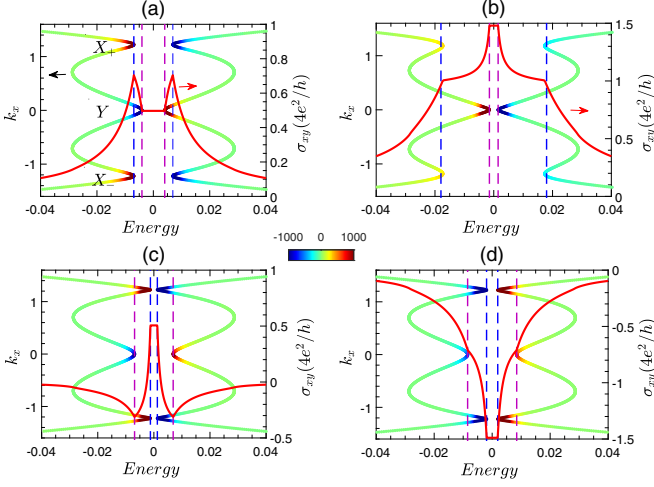
FIG. 2. Relation between the dispersion (left axis) and Hall conductivity (right axis) for (a) $\varphi = \pi/2$, $k_A = 0.02$, (b) $\varphi = \pi/2$, $k_A = 0.05$, (c) $\varphi = -\pi/2$, $k_A = 0.03$, and (d) $\varphi = -\pi/2$, $k_A = 0.04$, where the dispersion is plotted along $k_y = (\beta k_x^2 - \delta_1)/v_F$. The filled colors of the dispersion represent the value of the Berry curvatures. The blue and purple dashed lines indicate the magnitude of the local energy gaps Δ_X and Δ_Y, respectively. The rest of the parameters are set as $v_F = 10$, $\alpha = 2$, $\beta = 0.2$, $\delta_0 = 0.3$, $\hbar\omega = 0.25$, and $m_z = 0.005$, where the energy is in unit of eV.

Floquet theory [32,60–62], the time-period-dependent Hamiltonian $\mathcal{H}(\boldsymbol{k}, t)$ in the off-resonant regime, i.e., $\alpha k_A^2/(\hbar\omega) \ll 1$, where the electronic structure is modified through virtual photon processes, can be reduced to an effective static form

$$\mathcal{H}_{\text{eff}}(\boldsymbol{k}) \simeq H(\boldsymbol{k}) + \sum_{n=1}^{\infty} \frac{1}{n\hbar\omega}[H_n(\boldsymbol{k}), H_{-n}(\boldsymbol{k})], \quad (3)$$

with $H_n(\boldsymbol{k}) = \frac{1}{T}\int_0^T \mathcal{H}(\boldsymbol{k}, t)e^{-in\omega t}dt$ and $T = 2\pi/\omega$. Subsequently, we can obtain the effective Hamiltonian

$$\mathcal{H}_{\text{eff}}(\boldsymbol{k}) = \boldsymbol{n}(\boldsymbol{k}) \cdot \boldsymbol{\sigma}, \quad (4)$$

in which $\boldsymbol{n}(\boldsymbol{k}) = (\beta k_x^2 - v_F k_y - \delta_1, \alpha k_x k_y - \alpha\kappa, m_{\boldsymbol{k}})$, $\delta_1 = \delta_0 - 4\lambda_\beta$, and $m_{\boldsymbol{k}} = \gamma(2\beta k_x^2 + v_F k_y + \lambda_\beta) + m_z$. For the sake of brevity, we noted $\kappa = \frac{k_A^2}{4}\sin^2\theta\sin 2\phi$, $\gamma = \alpha k_A^2 \sin\varphi\cos\theta/(\hbar\omega)$, and $\lambda_\beta = \beta k_A^2(1 - \sin^2\theta\cos^2\phi)/8$, in which $k_A = eA_0/\hbar$ captures the light intensity. The effective Hamiltonian for the rest of the three valleys can be obtained from Eq. (4) directly by the replacements $k_x \to k_x \cos\vartheta_n - k_y \sin\vartheta_n$, $k_y \to k_x \sin\vartheta_n + k_y \cos\vartheta_n$, and $\phi \to \phi + \vartheta_n$, with $\vartheta_n = n\pi/2$ and $n = 1, 2, 3$. The Fermi surface is outlined by the boundaries of the color-filled regions in Fig. 1(c).

As can be seen, for $\theta = 0$, the CPL, incident in the z direction, will renormalize the parameters $\delta_0 \to \delta_1$ and $m_z \to m_{\boldsymbol{k}}$. Importantly, the Dirac mass for the driven fermions becomes momentum dependent. As a result, the local energy gaps around the Dirac points, characterized by $\Delta_Y = m_z - \gamma(\delta_0 - 5\lambda_\beta)$ and $\Delta_X = m_z + \gamma(2\delta_0 - 7\lambda_\beta)$, are different in magnitude, which is also visible in Fig. 2. This is distinct from the case of constant Dirac mass and enables us to control the inverted gaps around Y and $X_\pm$ separately, so as to realize

rich topological phases. For $\theta \neq 0$, the renormalization of $k_x k_y \to k_x k_y - \kappa$ would move the Dirac points away from the axis and break the rotation symmetry.

Upon application of an external electric field $\boldsymbol{E} = E_j \hat{e}_j$, the charge current density is given by [37,81]

$$J_i = -\frac{e}{(2\pi)^2}\sum_{s=\pm}\int d^2\boldsymbol{k}\left(v_{\boldsymbol{k},i}^s + \frac{e}{\hbar}\epsilon_{ij}E_j\Omega_{\boldsymbol{k},ij}^s\right)f_{\boldsymbol{k},s}, \quad (5)$$

with $\hat{e}_j$ the electric field's unit vector and ϵ_{ij} the two-dimensional Levi-Cività antisymmetric tensor. $\boldsymbol{v}_{\boldsymbol{k}}^s = \nabla_{\boldsymbol{k}}\varepsilon_{\boldsymbol{k},s}/\hbar$ is the group velocity, $f_{\boldsymbol{k},s}$ represents the nonequilibrium electron distribution function, and

$$\Omega_{\boldsymbol{k},ij}^s \equiv -s\frac{\boldsymbol{n}(\boldsymbol{k})}{2|\boldsymbol{n}(\boldsymbol{k})|^3} \cdot \left[\frac{\partial\boldsymbol{n}(\boldsymbol{k})}{\partial k_i} \times \frac{\partial\boldsymbol{n}(\boldsymbol{k})}{\partial k_j}\right] \quad (6)$$

defines the Berry curvature. For a relatively weak electric field, the nonequilibrium electron distribution function can be expanded as $f_{\boldsymbol{k},s} = \sum_{m=0}^{\infty} f_m$, where the subscript m marks the order of the electric field. Within the framework of the Boltzmann theory [37], it is easy to obtain the recurrence relation $f_0 = f(\varepsilon_{\boldsymbol{k}})$ and $f_{n\geqslant 1} = e\tau_{\boldsymbol{k}}\hbar^{-1}\boldsymbol{E}\cdot\nabla_{\boldsymbol{k}}f_{n-1}$, with $\tau_{\boldsymbol{k}}$ being the electron relaxation time due to the impurity scattering and $f(\varepsilon_{\boldsymbol{k}}) = [1 + e^{(\varepsilon_{\boldsymbol{k}} - E_F)/k_B T}]^{-1}$ is the Fermi-Dirac distribution function.

III. CPL-MODULATED LINEAR AHE

According to Eq. (5), we can define the linear conductivity tensor $\sigma_{ij} = \sigma_{D,ij} + \sigma_{B,ij}$, where

$$\sigma_{D,ij} = -e^2\sum_{s=\pm}\int\frac{d^2\boldsymbol{k}}{(2\pi)^2}v_{\boldsymbol{k},i}^s v_{\boldsymbol{k},j}^s\frac{\partial f(\varepsilon_{\boldsymbol{k},s})}{\partial\varepsilon_{\boldsymbol{k},s}}\tau_{\boldsymbol{k}}, \quad (7)$$

$$\sigma_{B,ij} = -\frac{e^2}{\hbar}\sum_{s=\pm}\int\frac{d^2\boldsymbol{k}}{(2\pi)^2}\epsilon_{ij}\Omega_{\boldsymbol{k},ij}^s f(\varepsilon_{\boldsymbol{k},s}), \quad (8)$$

represent respectively the Drude component of the conductivity and the linear Hall conductivity due to the Berry curvature. It should be noted that Eq. (8) is most valid for equilibrium dc Hall conductivity. In nonequilibrium, due to the nonuniversal nature of the Fermi-Dirac distribution, the Hall conductivity depends on the details of the system and its environment [69–72]. Here, we neglect the dissipative effects and consider the limit of high-frequency driving, where the effective Hamiltonian approach fully captures the topological features of Floquent-Bloch bands. In this case, the existence of topological edge states at sample boundaries could be inferred by computing the standard nondriven system invariants for the Floquet bands and the Chern number of the effective Hamiltonian can be interpreted as the Hall conductivity [64]. Strong drive amplitudes may lead to new topological transitions, which are not captured by the perturbative arguments discussed here.

The different topological phases can be distinguished by the Chern number of the valence band $C = \frac{1}{2\pi}\int_{BZ}\Omega_{\boldsymbol{k},xy}^- d^2\boldsymbol{k}$, which manifests in the AHE as the quantized Hall conductivity $\sigma_{xy} = Ce^2/h$ when the Fermi level is within the bulk band gap. By the expression of $\boldsymbol{n}(\boldsymbol{k})$ below Eq. (4), we can derive

$$\Omega_{\boldsymbol{k},xy}^s = -s\alpha\frac{m_z\xi_{\boldsymbol{k}} + \gamma[(\lambda_\beta + 2\delta_1)\xi_{\boldsymbol{k}} + 3v_F k_y\zeta_{\boldsymbol{k}} + \beta_\kappa]}{2[(\zeta_{\boldsymbol{k}} - v_F k_y)^2 + \alpha^2(k_x k_y - \kappa)^2 + m_{\boldsymbol{k}}^2]^{3/2}}, \quad (9)$$

in which $\xi_k = 2\beta k_x^2 + v_F k_y$, $\zeta_k = \beta k_x^2 - \delta_1$, and $\beta_\kappa = 6v_F\beta\kappa k_x$. The distribution of the Berry curvature is plotted in Figs. 1(a)–1(c), which is indicated by the filled colors in the dispersion. Here, as different from conventional semimetals, the Dirac mass in the numerator of the right hand side of Eq. (9), even in the absence of the CPL, is always tied to a momentum-dependent factor ξ_k. Consequently, the topological properties of the system depend strongly on location of the Dirac valleys in momentum space, because the sign of the Berry curvatures is determined jointly by the signs of m_z and ξ_k. For linearly polarized light, the term tied to γ in Eq. (9) vanishes, since $\gamma \propto \sin\varphi = 0$, which implies that the linearly polarized light cannot modulate the topological transitions. Below, we would mainly discuss the case for the CPL, i.e., $\varphi = \pm\pi/2$.

The numerical results for the anomalous Hall conductivity in the absence of the CPL are displayed in Figs. 1(d) and 1(e). Without the Dirac mass, the spectrum is gapless and the Berry curvature is vanishing, so that $\sigma_{xy} = 0$. For a finite Dirac mass, the spectrum will open a gap around the Dirac points and then the Hall conductivity exhibits a quantized plateau when the Fermi level is within the gap. If $\delta_0 < 0$, the system possesses only one inverted gap locating around Dirac point Y, as shown by Fig. 1(a), which results in a $2e^2/h$ Hall plateau; see Fig. 1(d). As δ_0 is varied from negative to positive, one would expect the system to experience a topological transition, because another two inverted gaps around Dirac points $X_\pm$ will be included; see Fig. 1(b) and the dispersion (left axis) in Fig. 1(e). However, curiously, the Hall conductivity remains unchanged during this procedure, as comparing Fig. 1(e) with Fig. 1(d).

To understand this anomalous phenomenon, let us focus on the neighborhood of the Dirac points, around which the Hamiltonian can be linearly approximated as $H_Y(q) = -v_F q_y \sigma_x - \alpha\frac{\delta_1}{v_F}q_x\sigma_y + \Delta_Y\sigma_z$ and $H_{X,\pm}(q) = \pm\sqrt{\delta_1/\beta}(2\beta q_x\sigma_x + \alpha q_y\sigma_y) + \Delta_X\sigma_z$, where the wave vector q is measured from the Dirac points. The corresponding Chern numbers can be easily determined as $C_Y = -\frac{1}{2}\text{sgn}(\delta_1)\text{sgn}(\Delta_Y)$ and $C_{X,\pm} = \frac{1}{2}\theta(\delta_1)\text{sgn}(\Delta_X)$, in which $\theta(x)$ is the unit step function. The Chern number for the present valley is $C = C_X + C_Y$ with $C_X = C_{X,+} + C_{X,-}$. The total Chern number C_4 of the system with four fourfold-rotation-related valleys can be obtained immediately through multiplying C by 4 [50]. Without the CPL, $\delta_1 = \delta_0$ and $\Delta_X = \Delta_Y = m_z$. For $\delta_0 < 0$, $C_{X,\pm} = 0$ and thus only the inverted gap around Y contributes to the Chern number, i.e., $C = C_Y = \text{sgn}(m_z)/2$. For $\delta_0 > 0$, the inverted gaps around $X_\pm$ contribute an additional Chern number $C_X = \text{sgn}(m_z)$. Besides, as δ_0 changes sign, C_Y reverses its sign as well, i.e., $C_Y = -\text{sgn}(m_z)/2$, demonstrated by Fig. 1(b) where the Berry curvatures around Y possess opposite sign with respect to Fig. 1(a). As a consequence, $C = \text{sgn}(m_z)/2$ remains unchanged with δ_0 changing sign. Therefore, in the absence of the CPL, the two situations for $\delta_0 < 0$ and $\delta_0 > 0$, though belonging to different topological phases, cannot be distinguished by evolution of the Chern number with respect to δ_0.

Additionally, since the local inverted gaps around different Dirac points are the same in magnitude for constant Dirac mass, the closing and reopening of them are always
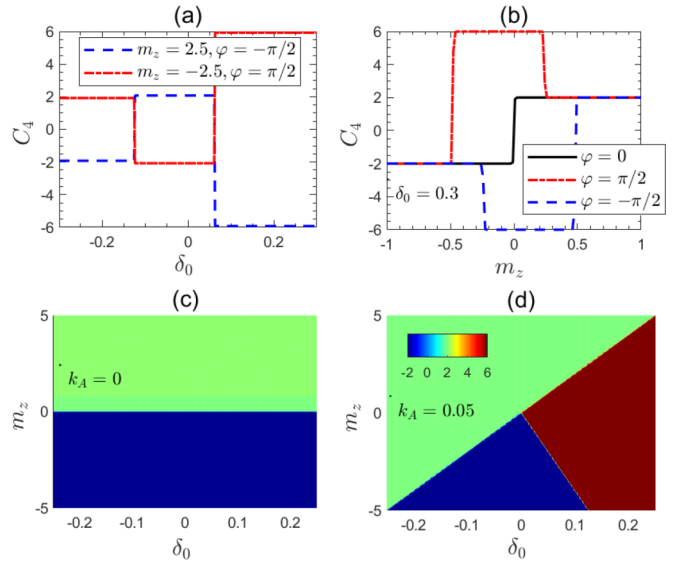

FIG. 3. Evolution of the total Chern number C_4 of the system in m_z-δ_0 parameter space, with (a), (b) $k_A = 0.01$, (c) $k_A = 0$, and (d) $\varphi = \pi/2$, $k_A = 0.05$, where m_z was magnified a thousand times. Other parameters are the same as in Fig. 2.

synchronous. As a result, the total Chern number $C_4 = 4\theta(\delta_1)\text{sgn}(\Delta_X) - 2\text{sgn}(\delta_1)\text{sgn}(\Delta_Y)$, in spite of many topological phases in the m_z-δ_0 parameter space, is either positive or negative 2 depending only on the sign of m_z; see the numerical results in Fig. 3(c). Interestingly, upon application of the CPL, Δ_X can be unequal to Δ_Y, so that we can control the inverted gaps around Y and $X_\pm$ independently. By tuning the CPL parameters, we can modulate the Hall plateau ranging from $\sigma_{xy} = -6e^2/h$ to $\sigma_{xy} = 6e^2/h$, illustrated by Figs. 2 and 3.

Furthermore, from Fig. 2(a), we observe that the CPL-modulated AHE exhibits an anomalous behavior, namely, as the Fermi level is tuned away from the gap, the Hall conductivity, instead of monotonically decreasing that occurs in static systems, will increase first to a maximum before decreasing. This nonmonotonic behavior can be understood as follows. The Hall conductivity within the bulk band gap is contributed by the valence band, which includes contribution of the inverted gaps around both Dirac points $X_\pm$ and Y. For $\delta_0 > 0$ and $m_z > 0$ in Fig. 2(a), the Berry curvatures of the valence band are positive around $X_\pm$ but negative around Y. Hence, the net Hall conductivity is positive $2e^2/h$ when E_F is within the gap. For a finite k_A and $\varphi = \pi/2$, Δ_Y reduces while Δ_X increases, such that the bulk band gap is determined by Δ_Y and the Hall plateau $\sigma_{xy} = 2e^2/h$ is of width $2|\Delta_Y|$. For $E_F > |\Delta_Y|$, the conduction band around Y, with positive Berry curvatures [see Fig. 2(a)], will be included first and contribute a positive Hall conductivity. So, the Hall conductivity increases. When $E_F > |\Delta_X|$, the conduction band around $X_\pm$, where the Berry curvatures are negative, is included as well, making the Hall conductivity decrease. Therefore, the Hall conductivity reaches its maximum at $|E_F| = |\Delta_X|$.

As k_A further increases, the gap around Y is closed when $\Delta_Y = 0$ and reopened for $\Delta_Y < 0$; after that C_Y changes sign again, as demonstrated in Fig. 2(b) where the Berry

curvatures around Y change sign with respect to Fig. 2(a). Then, the Berry curvatures of the valence band are positive for all the Dirac subvalleys and thus the Hall conductivity plateau turns out to be $\sigma_{xy} = 6e^2/h$ when E_F is within the bulk band gap. With the bulk band gap narrowing, the Berry curvatures, indicated by Fig. 2(b), distribute sharply at the edge of the conduction/valence band. As a result, in Fig. 2(b), the Hall conductivity changes slowly when $|E_F|$ is in the vicinity of Δ_X but increases rapidly for $|E_F| \to \Delta_Y$, forming a step-shaped structure around $\sigma_{xy} = 4e^2/h$. Consequently, we can observe a three-plateau structure of the Hall conductivity for some suitable parameters. If we reverse the polarization of the CPL, e.g., $\varphi = -\pi/2$ in Figs. 2(c) and 2(d), the behavior of Δ_X and Δ_Y will interchange, namely, Δ_X decreases and Δ_Y increases with the increment on k_A. As k_A increase, the gaps around $X_\pm$ will, simultaneously, be closed ($\Delta_X = 0$) and reopened ($\Delta_X < 0$); after that the Berry curvatures change sign around $X_\pm$, leading to a change of $8e^2/h$ in the Hall conductivity plateau, as compared in Figs. 2(c) and 2(d), also shown by Figs. 3(a) and 3(b).

As analyzed above, for constant Dirac mass, the Hall conductivity is δ_0 independent. However, as the CPL is turned on, the parameter δ_0 will enter Δ_X and Δ_Y, making the Hall plateau tunable by δ_0. As a consequence, in the presence of the CPL, varied topological phases can be observable in the m_z-δ_0 parameter space, as shown by Fig. 3(d). If $m_z \in \gamma(7\lambda_\beta - 2\delta_0, \delta_0 - 5\lambda_\beta)$, $|C_4| = 6$, otherwise $|C_4| = 2$. The phase boundaries $m_z = \gamma(\delta_0 - 5\lambda_\beta)$ and $m_z = \gamma(7\lambda_\beta - 2\delta_0)$, corresponding to $\Delta_Y = 0$ and $\Delta_X = 0$, are consistent with the analytical results. As the parameter moves across $\Delta_Y = 0$, only one inverted gap is closed and reopened, so that C_4 changes to 4, while if the parameter passes through $\Delta_X = 0$, two inverted gaps are simultaneously closed and reopened, and therefore, C_4 changes to 8.

As the Fermi level is out of the gap, the Drude component of the conductivity, shown by Figs. 4(a) and 4(b), could also contribute to the transverse conductivity. The Drude component of the transverse conductivity comes from the anisotropy, which follows the general relation $\sigma_{D,xy} = (\sigma_{D,xx} - \sigma_{D,yy}) \sin\phi \cos\phi$, as indicated by Fig. 4(b). Although the valleys with a banana-shaped Fermi surface exhibits the anisotropy, the net Drude component of the transverse conductivity, in the absence of the CPL or even with the CPL incident in the z direction ($\theta = 0$), vanishes because of the fourfold rotation symmetry, which is illustrated by the dark dashed lines in Figs. 4(a) and 4(b). When the incident direction of the CPL is tilted away from the z axis ($\theta \neq 0$), the fourfold rotation symmetry is broken and then nonzero $\sigma_{D,xy}$ can emerge, whose profile resembles the density of states (DOS) plotted in Fig. 4(d). The Drude component of the Hall conductivity exhibits a 2π-periodic oscillation with respect to ϕ, which is nonvanishing when the CPL is out of the x-z and y-z planes.

In Fig. 4(c), we also display the numerical results for the longitudinal conductivity. It is well known that the longitudinal conductivity relates closely to the DOSs at the Fermi level. As expected, the longitudinal conductivity is totally suppressed when the Fermi level is within the gap. As the Fermi energy is tuned away from the gap, the longitudinal conductivity increases linearly for relatively small E_F, due
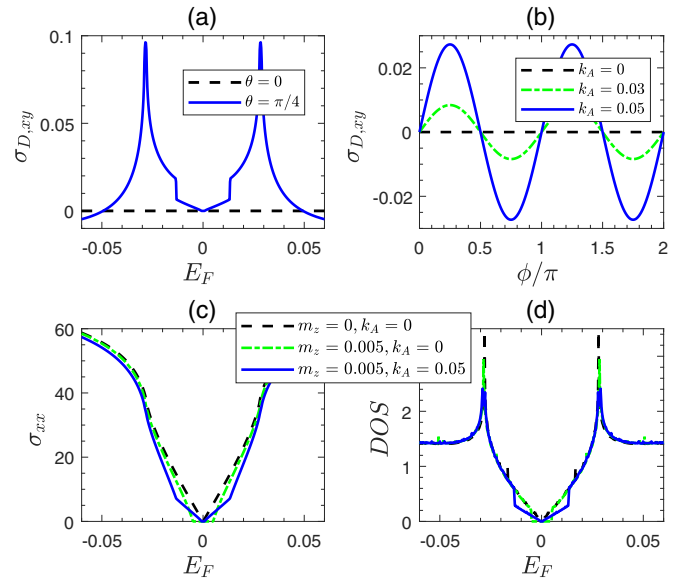

FIG. 4. The Drude component of the transverse conductivity vs the (a) Fermi energy for $\phi = \pi/4$, $k_A = 0.05$, and (b) azimuthal angle ϕ of the CPL for $\theta = \pi/4$. (c) The longitudinal conductivity and (d) DOSs as functions of the Fermi energy. The parameters are the same as in Fig. 2.

to the linear dispersion around the Dirac points. For constant Dirac mass, the local gaps for different Dirac points are the same in magnitude and the conductivity increases smoothly, as shown by the green dashed-dotted line. With the CPL turned on, these local gaps will be separated in magnitude. Then, the Fermi level first crosses only one Dirac cone when $\Delta_Y < |E_F| < \Delta_X$, and the other two Dirac cones are included when $|E_F| > \Delta_X$. As a result, the conductivity exhibits a vertex at $|E_F| = \Delta_X$, as seen from the blue-solid line in Fig. 4(c).

IV. CPL-MODULATED NONLINEAR AHE

While the linear AHE due to the Berry curvature decays rapidly when the Fermi level is away from the bulk band gap, the Berry curvature dipole would contribute to the nonlinear Hall effect as the Fermi level is out of the gap. Usually, the nonlinear Hall effect can exist in systems with TR symmetry, but requires breaking the inversion symmetry [74–80]. In the constant relaxation time approximation, the nonlinear charge current density, according to Eq. (5), can be written as $J_i^N = J_{D,i}^N + \frac{e^3\tau}{\hbar}\epsilon_{ij}D_b^{ij}E_jE_b$, where

$$D_b^{ij} = -\sum_{s=\pm} \int \frac{d^2k}{(2\pi)^2} \Omega_{k,ij}^s \upsilon_{k,b}^s \frac{\partial f(\varepsilon_{k,s})}{\partial \varepsilon_{k,s}} \qquad (10)$$

is the Berry curvature dipole and

$$J_{D,i}^N = \frac{e^3\tau^2}{\hbar} \sum_{s=\pm} \int \frac{d^2k}{(2\pi)^2} \frac{\partial \upsilon_{k,i}^s}{\partial k_j} \upsilon_{k,b}^s \frac{\partial f(\varepsilon_{k,s})}{\partial \varepsilon_{k,s}} E_jE_b \qquad (11)$$

contributes the Drude component of the nonlinear conductivity. We have used the Einstein summation convention for convenience. In the following, we focus only on the contribution from the Berry curvature dipole. After integration by
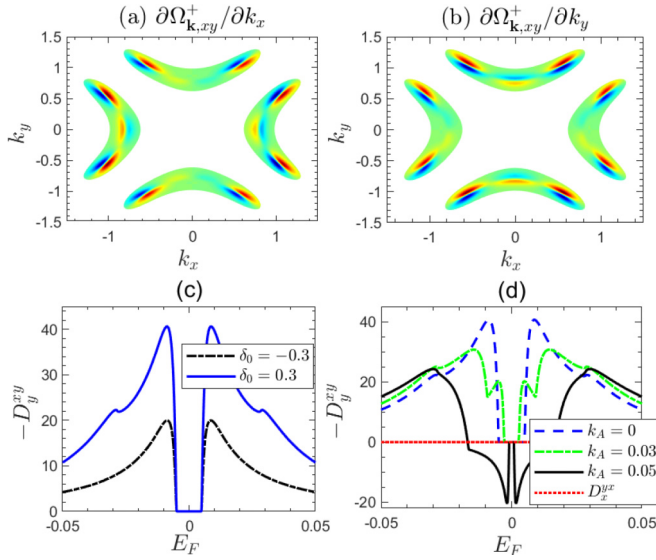
FIG. 5. Derivative of the Berry curvature $\Omega_{\mathbf{k},xy}^{+}$ with respect to (a) k_x and (b) k_y. (c), (d) Evolution of the Berry curvature dipole with (c) $k_A = 0$, $\delta_0 = -0.3, 0.3$ and (d) $\delta_0 = 0.3$, $k_A = 0, 0.03, 0.05$, for the valley described by Eq. (4). The rest of the parameters are the same as in Fig. 2.

parts, the nonvanishing Berry curvature dipole can be reexpressed as

$$D_b^{ij} = \sum_{s=\pm} \int \frac{d^2\mathbf{k}}{(2\pi)^2} \frac{\partial \Omega_{\mathbf{k},ij}^s}{\partial k_b} f(\varepsilon_{\mathbf{k},s}). \quad (12)$$

It shows that the Berry curvature dipole relies crucially on the symmetry of the Berry curvature. For Eq. (4), corresponding to the top banana-shaped region in Figs. 5(a) and 5(b), the Berry curvature dipole D_x^{yx}, in the absence of the CPL or with the CPL incident perpendicularly, can be expected to be vanishing, since $\Omega_{\mathbf{k},xy}^s$, indicated by Eq. (9), is even with respect to k_x. In other words, $\partial \Omega_{\mathbf{k},xy}^s / \partial k_x$ is an odd function of k_x, as shown by Fig. 5(a), whose integral over the wave vector vanishes. However, D_y^{xy} is nonvanishing, because $\partial \Omega_{\mathbf{k},xy}^s / \partial k_y$ is even vs k_x within the banana-shaped Fermi surface; see Fig. 5(b). This can be verified by the numerical results in Figs. 5(c) and 5(d). It means that, when the electric field is applied along direction y, one can observe charge current flowing along the x direction, while there is no transverse current when the electric field is along the x direction. The situation is the same for the bottom banana-shaped region of Figs. 5(a) and 5(b), but the Berry curvature dipole is of opposite sign. For the left and right banana-shaped regions, the cases are reversed, namely, there is (no) transverse current if the electric field is along the x (y) direction.

The Berry curvature dipole has a topological origin and also can witness the topological phase transition process. As seen from Fig. 5(d), with k_A varied from zero to 0.05, D_y^{xy} changes its sign in the vicinity of the boundary of the bands, as a response to the gap closing and reopening around the

Dirac point Y, indicating the topological transition. This is consistent with the results presented in Figs. 2(a) and 2(b). Although the banana-shaped Fermi surface of a single valley is asymmetric in the k_x or k_y direction, it should be noted that the Berry curvature dipoles between different valleys possess the symmetry $D_y^{xy} = -D_y^{xy}|_{\vartheta_n \to \vartheta_n + \pi}$, as reflected by the distribution of $\partial \Omega_{\mathbf{k},xy}^s / \partial k_{x,y}$ in Figs. 5(a) and 5(b). Consequently, the Berry curvature dipoles from opposite valleys may cancel each other out. Nevertheless, the Berry curvature dipole is sensitive to inversion-broken perturbations and we can predict that the Berry-curvature-dipole-induced nonlinear Hall effect can be observable in type-II SDSMs, if the inversion symmetry is, for example, further broken by strain or other perturbations.

V. CONCLUSIONS AND REMARKS

In summary, we have studied the photon-modulated linear and nonlinear AHE in type-II SDSMs and found that rich topological phases and interesting transport phenomena associated with the topological phase transitions can be realized and manipulated by the CPL. Because the local inverted gaps around different Dirac points respond differently to the CPL, we can modulate the topological phase transition conveniently. By tuning the CPL parameters, the QAH plateau within the bulk band gap can be modulated ranging $-6e^2/h$ to $6e^2/h$. The interplay between the Dirac points also can be regulated by the CPL, which results in anomalous behaviors in the anomalous Hall conductivity. Due to the strong anisotropy of the electronic structure, we demonstrate that, while the Berry-curvature-induced AHE is strongly suppressed as the Fermi level is away from the bulk band gap, the Drude component of the conductivity would contribute to the AHE. Besides, the nonlinear Hall effect because of the Berry curvature dipole can be observable when the inversion symmetry is broken. In experiments, in order not to destroy the material while still providing measurable signal, by the recently developed ultrafast laser pulse driving and on-chip detecting techniques [73], our proposal could be realizable with the midinfrared light, the photon energy of which can be large compared with the higher-energy cutoff for the present 2D semi-Dirac cone [50].

[1] N. Nagaosa, J. Sinova, S. Onoda, A. H. MacDonald, and N. P. Ong, Rev. Mod. Phys. **82**, 1539 (2010).

[2] R. Karplus and J. M. Luttinger, Phys. Rev. **95**, 1154 (1954).

[3] J. Smit, Physica **21**, 877 (1955).

[4] J. Smit, Physica **24**, 39 (1958).

[5] E. M. Pugh and N. Rostoker, Rev. Mod. Phys. **25**, 151 (1953).

[6] G. Sundaram and Q. Niu, Phys. Rev. B **59**, 14915 (1999).

[7] M. Onoda and N. Nagaosa, J. Phys. Soc. Jpn. **71**, 19 (2002).

[8] T. Jungwirth, Q. Niu, and A. H. MacDonald, Phys. Rev. Lett. **88**, 207208 (2002).

[9] D. Culcer, A. MacDonald, and Q. Niu, Phys. Rev. B **68**, 045327 (2003).

[10] L. Berger, Phys. Rev. B **2**, 4559 (1970).

[11] L. Berger, Physica **30**, 1141 (1964).

[12] P. N. Dheer, Phys. Rev. **156**, 637 (1967).

[13] Y. Tian, L. Ye, and X. Jin, Phys. Rev. Lett. **103**, 087206 (2009).

[14] T. Miyasato, N. Abe, T. Fujii, A. Asamitsu, S. Onoda, Y. Onose, N. Nagaosa, and Y. Tokura, Phys. Rev. Lett. **99**, 086602 (2007).

[15] H. Ishizuka and N. Nagaosa, Sci. Adv. **4**, eaap9962 (2018).

[16] S.-Y. Yang, Y. Wang, B. R. Ortiz, D. Liu, J. Gayles, E. Derunova, R. Gonzalez-Hernandez, L. Šmejkal, Y. Chen, S. S. P. Parkin, S. D. Wilson, E. S. Toberer, T. McQueen, and M. N. Ali, Sci. Adv. **6**, eabb6003 (2020).

[17] N. Manyala, Y. Sidis, J. F. DiTusa, G. Aeppli, D. P. Young, and Z. Fisk, Nat. Mater. **3**, 255 (2004).

[18] T. Liang, J. Lin, Q. Gibson, S. Kushwaha, M. Liu, W. Wang, H. Xiong, J. A. Sobota, M. Hashimoto, P. S. Kirchmann, Z.-X. Shen, R. J. Cava, and N. P. Ong, Nat. Phys. **14**, 451 (2018).

[19] M. Z. Hasan and C. L. Kane, Rev. Mod. Phys. **82**, 3045 (2010).

[20] X.-L. Qi and S.-C. Zhang, Rev. Mod. Phys. **83**, 1057 (2011).

[21] N. P. Armitage, E. J. Mele, and A. Vishwanath, Rev. Mod. Phys. **90**, 015001 (2018).

[22] R. Yu, W. Zhang, H.-J. Zhang, S.-C. Zhang, X. Dai, and Z. Fang, Science **329**, 61 (2010).

[23] C.-Z. Chang, J. Zhang, X. Feng, J. Shen, Z. Zhang, M. Guo, K. Li, Y. Ou, P. Wei, L.-L. Wang, Z.-Q. Ji, Y. Feng, S. Ji, X. Chen, J. Jia, X. Dai, Z. Fang, S.-C. Zhang, K. He, Y. Wang *et al.*, Science **340**, 167 (2013).

[24] C.-Z. Chang, W. Zhao, D. Y. Kim, H. Zhang, B. A. Assaf, D. Heiman, S.-C. Zhang, C. Liu, M. H. W. Chan, and J. S. Moodera, Nat. Mater. **14**, 473 (2015).

[25] S. Nakatsuji, N. Kiyohara, and T. Higo, Nature (London) **527**, 212 (2015).

[26] A. J. Bestwick, E. J. Fox, X. Kou, L. Pan, K. L. Wang, and D. Goldhaber-Gordon, Phys. Rev. Lett. **114**, 187201 (2015).

[27] C.-X. Liu, S.-C. Zhang, and X.-L. Qi, Annu. Rev. Condens. Matter Phys. **7**, 301 (2016).

[28] M.-X. Deng, W. Luo, W. Y. Deng, M. N. Chen, L. Sheng, and D. Y. Xing, Phys. Rev. B **94**, 235116 (2016).

[29] D. Maryenko, A. S. Mishchenko, M. S. Bahramy, A. Ernst, J. Falson, Y. Kozuka, A. Tsukazaki, N. Nagaosa, and M. Kawasaki, Nat. Commun. **8**, 14777 (2017).

[30] Q. Wang, Y. Xu, R. Lou, Z. Liu, M. Li, Y. Huang, D. Shen, H. Weng, S. Wang, and H. Lei, Nat. Commun. **9**, 3681 (2018).

[31] S. N. Guin, K. Manna, J. Noky, S. J. Watzman, C. Fu, N. Kumar, W. Schnelle, C. Shekhar, Y. Sun, J. Gooth, and C. Felser, NPG Asia Mater. **11**, 16 (2019).

[32] X.-S. Li, C. Wang, M.-X. Deng, H.-J. Duan, P.-H. Fu, R.-Q. Wang, L. Sheng, and D. Y. Xing, Phys. Rev. Lett. **123**, 206601 (2019).

[33] D.-W. Zhang, Y.-Q. Zhu, Y. X. Zhao, H. Yan, and S.-L. Zhu, Adv. Phys. **67**, 253 (2018).

[34] M.-X. Deng, G. Y. Qi, R. Ma, R. Shen, R.-Q. Wang, L. Sheng, and D. Y. Xing, Phys. Rev. Lett. **122**, 036601 (2019).

[35] X.-D. Hu, L.-Y. Li, Z.-X. Guo, and Z. Li, New J. Phys. **23**, 073031 (2021).

[36] F. D. M. Haldane, Phys. Rev. Lett. **61**, 2015 (1988).

[37] D. Xiao, M.-C. Chang, and Q. Niu, Rev. Mod. Phys. **82**, 1959 (2010).

[38] C.-X. Liu, X.-L. Qi, X. Dai, Z. Fang, and S.-C. Zhang, Phys. Rev. Lett. **101**, 146802 (2008).

[39] Z. Qiao, S. A. Yang, W. Feng, W.-K. Tse, J. Ding, Y. Yao, J. Wang, and Q. Niu, Phys. Rev. B **82**, 161414(R) (2010).

[40] H. Zhang, C. Lazo, S. Blügel, S. Heinze, and Y. Mokrousov, Phys. Rev. Lett. **108**, 056802 (2012).

[41] K. F. Garrity and D. Vanderbilt, Phys. Rev. Lett. **110**, 116802 (2013).

[42] Z. F. Wang, Z. Liu, and F. Liu, Phys. Rev. Lett. **110**, 196801 (2013).

[43] H. Zhang, J. Wang, G. Xu, Y. Xu, and S.-C. Zhang, Phys. Rev. Lett. **112**, 096804 (2014).

[44] K. F. Garrity and D. Vanderbilt, Phys. Rev. B **90**, 121103(R) (2014).

[45] H. Zhang, H. Huang, K. Haule, and D. Vanderbilt, Phys. Rev. B **90**, 165143 (2014).

[46] K. Saha, Phys. Rev. B **94**, 081103(R) (2016).

[47] V. Pardo and W. E. Pickett, Phys. Rev. Lett. **102**, 166803 (2009).

[48] V. Pardo and W. E. Pickett, Phys. Rev. B **81**, 035111 (2010).

[49] S. Banerjee, R. R. P. Singh, V. Pardo, and W. E. Pickett, Phys. Rev. Lett. **103**, 016402 (2009).

[50] H. Huang, Z. Liu, H. Zhang, W. Duan, and D. Vanderbilt, Phys. Rev. B **92**, 161115(R) (2015).

[51] A. S. Rodin, A. Carvalho, and A. H. Castro Neto, Phys. Rev. Lett. **112**, 176801 (2014).

[52] A. Kobayashi, Y. Suzumura, F. Piéchon, and G. Montambaux, Phys. Rev. B **84**, 075450 (2011).

[53] Y. Wu, Opt. Express **22**, 1906 (2014).

[54] P. Dietl, F. Piéchon, and G. Montambaux, Phys. Rev. Lett. **100**, 236405 (2008).

[55] T. Oka and H. Aoki, Phys. Rev. B **79**, 081406(R) (2009).

[56] T. Kitagawa, T. Oka, A. Brataas, L. Fu, and E. Demler, Phys. Rev. B **84**, 235108 (2011).

[57] Y. H. Wang, H. Steinberg, P. Jarillo-Herrero, and N. Gedik, Science **342**, 453 (2013).

[58] E. J. Sie, J. W. McIver, Y.-H. Lee, L. Fu, J. Kong, and N. Gedik, Nat. Mater. **14**, 290 (2015).

[59] F. Mahmood, C.-K. Chan, Z. Alpichshev, D. Gardner, Y. Lee, P. A. Lee, and N. Gedik, Nat. Phys. **12**, 306 (2016).

[60] M. S. Rudner, N. H. Lindner, E. Berg, and M. Levin, Phys. Rev. X **3**, 031005 (2013).

[61] P. Titum, N. H. Lindner, M. C. Rechtsman, and G. Refael, Phys. Rev. Lett. **114**, 056801 (2015).

[62] A. Farrell and T. Pereg-Barnea, Phys. Rev. Lett. **115**, 106403 (2015).

[63] T. Oka and S. Kitamura, Annu. Rev. Condens. Matter Phys. **10**, 387 (2019).

[64] M. S. Rudner and N. H. Lindner, Nat. Rev. Phys. **2**, 229 (2020).

[65] A. Kumar, M. Rodriguez-Vega, T. Pereg-Barnea, and B. Seradjeh, Phys. Rev. B **101**, 174314 (2020).

[66] F. Giustino, J. H. Lee, F. Trier, M. Bibes, S. M. Winter, R. Valentí, Y.-W. Son, L. Taillefer, C. Heil, A. I. Figueroa, B. Plaçais, Q. Wu, O. V. Yazyev, E. P. A. M. Bakkers, J. Nygård,

P. Forn-Díaz, S. D. Franceschi, J. W. McIver, L. E. F. F. Torres, T. Low *et al.*, J. Phys.: Mater. **3**, 042006 (2021).

[67] L. Du, Q. Chen, A. D. Barr, A. R. Barr, and G. A. Fiete, Phys. Rev. B **98**, 245145 (2018).

[68] A. Huamán, L. E. F. Foa Torres, C. A. Balseiro, and G. Usaj, Phys. Rev. Research **3**, 013201 (2021).

[69] H. Dehghani, T. Oka, and A. Mitra, Phys. Rev. B **90**, 195429 (2014).

[70] H. Dehghani, T. Oka, and A. Mitra, Phys. Rev. B **91**, 155422 (2015).

[71] L. E. F. Foa Torres, P. M. Perez-Piskunow, C. A. Balseiro, and G. Usaj, Phys. Rev. Lett. **113**, 266801 (2014).

[72] A. Kundu, H. A. Fertig, and B. Seradjeh, Phys. Rev. Lett. **113**, 236803 (2014).

[73] J. W. McIver, B. Schulte, F.-U. Stein, T. Matsuyama, G. Jotzu, G. Meier, and A. Cavalleri, Nat. Phys. **16**, 38 (2020).

[74] I. Sodemann and L. Fu, Phys. Rev. Lett. **115**, 216806 (2015).

[75] Z. Z. Du, C. M. Wang, H.-Z. Lu, and X. C. Xie, Phys. Rev. Lett. **121**, 266601 (2018).

[76] P. A. Pantaleón, T. Low, and F. Guinea, Phys. Rev. B **103**, 205403 (2021).

[77] M.-X. Deng, W. Y. Deng, D. X. Shao, R.-Q. Wang, R. Shen, L. Sheng, and D. Y. Xing, Phys. Rev. B **95**, 115102 (2017).

[78] W. Rao, Y.-L. Zhou, Y.-j. Wu, H.-J. Duan, M.-X. Deng, and R.-Q. Wang, Phys. Rev. B **103**, 155415 (2021).

[79] J. I. Facio, D. Efremov, K. Koepernik, J.-S. You, I. Sodemann, and J. van den Brink, Phys. Rev. Lett. **121**, 246403 (2018).

[80] P. Bhalla, M.-X. Deng, R.-Q. Wang, L. Wang, and D. Culcer, Phys. Rev. Lett. **127**, 206801 (2021).

[81] Y.-H. Lei, Y.-L. Zhou, H.-J. Duan, M.-X. Deng, Z.-E. Lu, and R.-Q. Wang, Phys. Rev. B **104**, L121117 (2021).